Interfacing Standalone Loads With Renewable Energy Source and Hybrid Energy Storage System Using a Dual Active Bridge Based Multi-Port Converter

Shashank Kurm, *Student Member, IEEE*, and Vivek Agarwal, *Fellow, IEEE*

***Abstract*— Batteries used for providing backup power in renewable energy sources (RES) fed standalone power systems often suffer from a limited lifetime because of high charging and discharging currents arising from sudden changes in load and/or generation. To prevent this, supercapacitors (SCs) are used to supply the high-frequency (HF) power surges. In this article, a new way of interfacing hybrid energy storage systems (HESSs) (Battery + SC) with RES and loads by employing a current fed dual active bridge (DAB) converter based multi-port converter (MPC) is proposed. The proposed approach enables the MPC to regulate the load voltage while tracking the maximum power point (MPP) of the RES and protecting the battery from transients arising from variations in load and/or renewable generation. The SC is used for tracking MPP so that the transient changes in RES generation do not cause a sudden rise/fall in the battery current. The employed MPC structure is designed in such a way that most of the power processing takes place in one stage only resulting in lower losses. The number of switches is reduced by merging the power conversion stages, which helps in keeping the cost low. Experimental results on a laboratory prototype under various static and dynamic conditions are presented.**

***Index Terms*— Current fed dual active bridge (DAB), hybrid energy storage systems (HESSs), multi-port converter (MPC), off-grid power systems, renewable energy system, supercapacitor (SC).**

I. Introduction

IN RENEWABLE energy-based standalone power systems, backup power sources such as batteries, fuel cells, diesel generators, and so on are required to negotiate the intermittency of renewable energy. Batteries are one of the most common sources of backup power. Batteries employed in such systems are frequently exposed to high magnitude currents which are much higher than the rated values [1], [2] due to sudden changes in loads and/or generation, thus significantly limiting their lifetime [3]–[10]. High magnitude loading usually lasts for a short time interval, and it is not economical to design the battery bank for such load currents, whose magnitude is usually several times higher than the steady-state value. To extend the lifetime of batteries, they can be complemented with supercapacitors (SCs), which are high power density energy storage devices and can supply the required high magnitude current. This combination supplies the transient and steady-state components of the load current without stressing out the battery. If SCs are present, the battery does not need to be designed for peak power requirement but only for the steady-state power requirement [4]–[10] thus leading to low weight/volume of the energy storage system (ESS). A combination of battery and SC can satisfy both the energy demand and the power demand of the load and is known as Hybrid ESS (HESS). Based on how the battery and SC are interfaced, the various configurations of HESS are.

A. Passive HESS (P-HESS)

In a P-HESS, the two energy storage devices are connected directly to each other without any interfacing converter as shown in Fig. 1(a) [3]. This is a cost-effective way, but there is no active control over the power sharing between the two energy storage sources and the voltage range of operation of SC is limited.

B. Semi-Active HESS (SA-HESS)

In an SA-HESS, one of the energy storage elements is interfaced to the load through a converter, whereas the other one is directly connected across load terminals. There are two types of SA-HESS which are shown in Fig. 1(b) and (c). In type A SA-HESS [4] [Fig. 1(b)], the battery is connected directly to load whereas the SC is interfaced via a power electronic converter. This allows SC to operate over a wide voltage range but the battery current, in this case, is not completely shielded from the transients. In a type B SA-HESS [5], [6] [Fig. 1(c)], the SC is connected directly across the load. This allows the battery current to reject the transients but the voltage range of operation of the SC is limited by load voltage regulation requirements.

C. Active HESS (A-HESS)

In an A-HESS, both the battery and the SC are interfaced with the load through individual power electronic converters.

Manuscript received 29 December 2020; revised 28 April 2021 and 19 August 2021; accepted 3 October 2021. Date of publication 7 October 2021; date of current version 2 August 2022. Recommended for publication by Associate Editor Maja Harfman Todorovic. *(Corresponding author: Shashank Kurm.)*

The authors are with the Department of Electrical Engineering, Indian Institute of Technology, Bombay, Mumbai 400076, India (e-mail: eekshashank@ee.iitb.ac.in; agarwal@ee.iitb.ac.in).

Color versions of one or more figures in this article are available at https://doi.org/10.1109/JESTPE.2021.3118462.

Digital Object Identifier 10.1109/JESTPE.2021.3118462

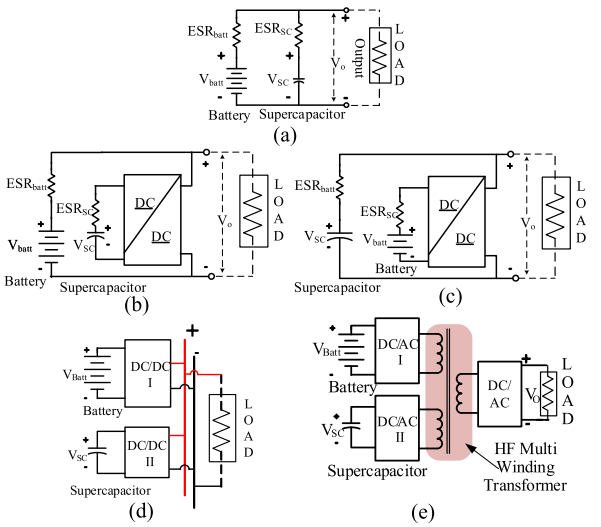

Fig. 1. Various configurations of HESS. (a) P-HESS [3], (b) type A SA-HESS [4], (c) type B SA-HESS [5], (d) conductively coupled A-HESS [7], and (e) magnetically coupled A-HESS. [10] $\mathbf{V_{batt}}$: battery voltage, $\mathbf{V_{SC}}$: SC voltage, $\mathbf{V_O}$: load voltage, $\mathbf{ESR_{batt}}$: equivalent series resistance (ESR) of battery, $\mathbf{ESR_{SC}}$: ESR of SC.

TABLE I
COMPARISON OF VARIOUS HESS CONFIGURATIONS

System	Voltage Boost Capability		Loss	Wide voltage range of SC	Control over Battery current
	V_{batt}	V_{SC}			
P-HESS	No	No	L	No	No
SA-HESS-A	No	Yes	M	Yes	No
SA-HESS-B	Yes	No	M	No	Yes
A-HESS	Yes	Yes	H	Yes	Yes

H= High, M= Medium, L= Low
NA: Supercapacitor connected without converter

This system offers control over the sharing of power between the two sources and the voltage of both sources can be boosted to match the load voltage. Depending on the type of coupling between the load and energy storage, an A-HESS can be either conductively coupled [7]–[9] or magnetically coupled [10] as shown in Fig. 1(d) and (e), respectively. Table I summarizes and compares the various types of HESS configurations.

Renewable energy sources (RES)-based standalone system should comprise a RES as the main energy source, ESS for backup power, and an SC bank to protect the battery from transient loading. The characteristics and objectives of the RES, battery, and SC impose the following requirements on the power electronic system designed to interface these elements with the load.

1) The maximum power point (MPP) of RES must be tracked.
2) Load voltage must be regulated to its nominal value under normal and transients loading conditions.
3) Transient components of power must be delivered/absorbed by the SC, and only the steady-state power be supplied or absorbed by the battery.
4) Power from the RES and battery should be processed once as multiple power processing stages reduce efficiency.

This work aims to interface HESS with an RES-powered standalone power system. The major contribution is to interface and control the various elements in the system, which includes an RES (solar PV), battery, and SC. All these elements have distinct requirements that must be fulfilled and offer distinct advantages that can be made use of. An integrated approach that takes SC operation into account for controlling the other elements of the system as well can enhance the system performance significantly. This article proposes one such approach in which the SC is used to perform MPP of the solar PV thus enabling it to take care of variation in RES generation. The battery current reference is obtained from power balance and SC energy management which is then controlled using CF-DAB operation. Using this approach all of the above-mentioned objectives are fulfilled.

To interface all the elements to the load while performing the above-mentioned functions, multi-port converters (MPCs) offer a low-cost solution compared to dedicated converters for individual sources as some of the components can be shared and non-critical or redundant power processing stages can be eliminated leading to higher efficiency [11], [12]. In an MPC, the coupling between the multiple elements can be either conductive [13], [14] or magnetic [15], [16], or both [17], [26]. Accordingly, these converters can be classified into conductively coupled MPC, magnetically coupled MPC, and hybrid MPC, which involve both conductive and magnetic coupling among the energy sources/loads. Conductively coupled or non-isolated MPCs, shown in Fig. 2(a), use a lower number of switches and are generally preferred where isolation is not required. Isolated MPCs combine the various sources/loads through a multi-winding high frequency (HF) transformer or multiple transformers. Dual active bridge (DAB) converters are a common form of HF link converters and can be extended to multiple ports using multi-winding transformers as shown in Fig. 2(b). Fully isolated MPCs have been proposed in [10], [15], and [16]. They require separate HF inverters for each port, resulting in a larger number of components which leads to increased system cost. Also, there is a circulating current between the windings, which increases the conduction losses.

Partially isolated MPCs, such as the one shown in Fig. 2(c) have both magnetic and conductive coupling [17]–[26]. They combine the low component count advantage of conductive coupled MPCs with the advantages of isolated MPCs such as high voltage gain and galvanic isolation. Qian *et al.* [20] have proposed one such multi-port dc/dc converter. However, in this converter, zero average voltage across the transformer is maintained using the width of the gate pulses to the switches. Any inaccuracy in the pulsewidth calculation or differences in device characteristics may lead to a non-zero average voltage across the transformer, leading to its saturation. Mangu *et al.* [22] have proposed an MPC for a solar PV and wind energy interfacing application. However, in this converter, power from the battery is processed in two stages,

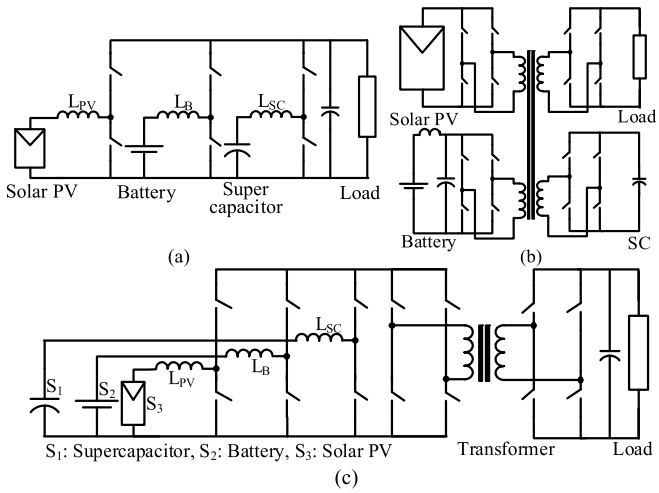

Fig. 2. Various types of MPCs: (a) conductively coupled or non-isolated, (b) magnetically coupled or isolated, and (c) mixed or hybrid coupled.

which increases the losses and thus translates to a lower battery run-time.

Current-fed DAB converters offer a multi-port structure and can be well exploited to form MPCs as demonstrated in [18], [21]–[26]. Lu *et al.* [23] and Sun *et al.* [24] have presented unidirectional MPCs based on current fed full-bridge converters, featuring two control variables. In these converters, the unidirectional nature restricts the battery to be charged from sources placed on the secondary side.

Most of the MPCs reported in the literature are aimed at interfacing only the RES and battery, or multiple RESs and storage. Interfacing of SC is different from interfacing multiple RESs from the control point of view and MPCs for SCs have not received enough attention in the literature. The conventional way of interfacing a HESS is to use a separate converter as presented in [7]. Here, the control of SC is done by extracting the HF component of load power demand and supplying it using the SC. The rest of the components of current can be supplied from other sources. Even though this approach protects the battery from transients due to load fluctuations, the transients caused due to sudden variation in renewable energy availability which may be caused by factors like the sudden appearance of clouds over the PV panels may not be filtered. In [25], a CF-DAB-based MPC is proposed to interface battery and SC to the load. In this scheme, the SC is on the high voltage side, and also the voltage range over which SC is operated is limited by the minimum pulsewidth of the voltage waveform across the transformer winding. This leads to the under-utilization of SC and/or necessitates a higher capacity SC for a given application.

The converter structure that is adopted in this work for interfacing all the elements is a partially isolated MPC. The proposed MPC exploits sharing of components to reduce the component count and to minimize the number of power processing stages while achieving all the desirable features discussed above. The core of the MPC is a current-fed DAB converter, which is configured to interface PV and battery to a common output. The SC is interfaced to the low voltage side using a non-isolated converter.

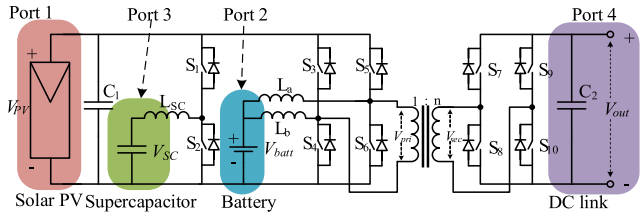

Fig. 3. Schematic of the MPC for interfacing HESS and RES to load. V_{PV}: solar panel voltage, V_{SC}: SC voltage, V_{batt}: battery voltage, V_{DC}: dc load voltage.

The rest of this article is organized as follows. Section II describes the proposed MPC and its various ports. Section III explains the control to achieve the various objectives and generation of gate signals for the switches. Section IV presents an analysis of the zero voltage switching (ZVS) region, current stresses, losses, and leakage current in the proposed MPC. Section V presents system designs and steps to select the various parameters. Section VI presents the experimental results collected on a laboratory prototype under various operating conditions. Section VII summarizes the contributions and concludes the article.

II. MPC: Ports and Objectives

Fig. 3 shows the schematic of the MPC structure used in this article. The core circuit for the MPC is a current-fed DAB (CF-DAB) converter where the battery is connected through two inductors to the poles of the two legs of the primary side HF inverter like an interleaved converter for controlling battery current. The capacitor C_1 can act as a variable voltage port and can be used to interface the PV. By controlling the voltage of capacitor $C_1(V_{C1})$, MPPT of PV can be carried out. This leads to a single-stage power transfer from the PV to the load. The SC is connected to C_1 through a separate bidirectional buck-boost converter. The various ports of the proposed converter and the associated requirements are.

A. RES (Solar) Port (Port 1)

The RES, most commonly a solar PV panel, is connected across the input side capacitor C_1 of the CF-DAB, and this is termed as *Port 1*. This port is voltage controlled, and the reference voltage is the MPP voltage of the RES. If the available RES is a wind turbine generator, it can be interfaced through an active/passive rectifier. This port can also be used to interface a fuel cell or a diesel generator as an alternate power source. However, this article will focus on solar PV applications. The PV array must be operated at its MPP whenever possible. When the power generated by the solar panel exceeds the load power, the excess power is diverted toward the battery for charging. Operation at MPP is performed by regulating V_{C1} equal to the MPP voltage of the PV denoted by V_{MPP}. V_{MPP} is obtained using MPP algorithms like perturb and observe or incremental conductance method.

B. Battery Port (Port 2)

To the switching node of S_3-S_4 and S_5-S_6, the battery pack is connected through inductors L_a and L_b and is termed as

Port 2. The minimum inductance values of L_a and L_b depend on the permissible ripple in the battery current and are

$$L_a^{\min}\left(L_b^{\min}\right) = \frac{V_{\text{batt}}(1 - D_{\max})}{2f\,\Delta I_{\text{batt}}^{\max}}. \tag{1}$$

The battery current must be regulated at all times and should be free from sharp rise and fall for long battery life. To protect the battery from the high magnitude and HF current, the battery current is controlled using switches S_3-S_6. These switches are the switches of the DAB primary side inverter, and also form an interleaved converter from the PV to the battery. Switches S_3-S_6 are operated to control the battery current and prevent it from power surges. The power supplied by the battery is given by

$$P_{\text{batt}} = V_{\text{batt}} I_{\text{batt}}. \tag{2}$$

I_{batt} is controlled such that the battery current does not experience sudden changes, and the battery is thus protected from surge loading.

C. SC Port (Port 3)

Since the battery does not supply the transient power demand of the load, the instantaneous difference between the load power and RES plus battery power is supplied by the SC. The SC is connected to the switching node of S_1-S_2 through inductor L_{SC} as shown in Fig. 3. This port is termed *Port 3*. Switches S_1-S_2 are operated to regulate the voltage of the capacitor C_1, which is also the PV voltage, V_{PV}. V_{PV} also determines the amplitude of the voltage at the transformer primary winding. MPPT is performed by regulating V_{PV} to V_{MPP} of the solar panel, using the SC as an energy buffer. Any sudden fall in PV power due to conditions such as shading is reflected in the SC power and not the battery. Thus, the battery is prevented from supplying the transient power that could be necessitated by a sudden change in insolation.

D. DC Load Port (Port 4)

The dc load, which can be either a standalone dc load or the dc link of an inverter feeding an ac load is connected to the dc link of the secondary side HF inverter and is termed as *Port 4*. The balance of power is maintained by regulating the output voltage of the MPC (V_{out}). The reference value of V_{out} is the nominal load voltage in the case of dc loads, whereas, in the case of ac loads, it is the nominal dc link voltage of the interfacing inverter. Load voltage regulation is done by the DAB stage of the proposed converter, by controlling the phase shift δ between the gate pulses of primary and secondary side HF inverters. The power transfer through a DAB converter is given by

$$P = \left(\frac{4}{\pi}\right)^2 \frac{V_1 V_2}{2\pi f L n} \sin(d_1\pi)\sin(d_2\pi)\sin(\phi)$$

where

$$\phi = (d_2 - d_1)\pi + 2\pi\delta \tag{3}$$

where d_1 and d_2 are the duty ratio of gate pulses for switches in the primary and secondary side bridges and δ is the phase difference between them. n is the turns ratio of the transformer, V_1 is the PV voltage (V_{PV}), V_2 is the load voltage, L is the net leakage inductance referred to the primary side, and f is the switching frequency.

The secondary side bridge of the DAB is switched at a duty ratio of 0.5. Regulation of V_{out} ensures power balance and is implemented by comparing V_{out} with the reference output voltage and generating δ using a PI controller. The power rating of the various ports and the transformer are given in Table II. It can be seen that in the proposed MPC, the power rating of the transformer is only the load power, and not the load plus battery charging power as in the case of fully isolated MPCs.

TABLE II
POWER RATINGS OF VARIOUS PORTS AND TRANSFORMER

Port/ element	Power rating
1 (RES)	P_{PV}^{max}
2 (Battery)	$\max((P_{PV}^{max} - P_{load}^{max}), P_{load}^{max})$
3 (SC)	P_{load}^{max}
4 (Load)	P_{load}^{max}
Transformer	P_{load}^{max}

III. OPERATION AND CONTROL

The operation and control of the proposed MPC are presented in this section. The parasitic resistances of switches and other elements, magnetizing current, core loss of transformer, and switching ripples in C_1 and C_2 are neglected.

A. Energy Management Algorithm

The PV is the main power source in the system and is operated at its MPP. When PV power (P_{PV}) exceeds the load demand (P_{load}), the excess power is used to charge the battery and when the PV generation is lower than the load, the deficit power is drawn from the battery. The SC ensures that the transient component of load current is not drawn from the battery. Since the energy storage capacity of the SC is less, it cannot act as an energy source/sink for a long time and is used only to source/sink transient power. The battery current I_{batt} is controlled such that it changes slowly toward the final value which depends on the power balance.

1) Control of S_1-S_2: The SC converter, consisting of S_1 and S_2 is operated to regulate the PV voltage (V_{C1}) equal to the MPPT voltage of the PV panel (V_{MPPT}), which is obtained using an adaptive perturb and observe algorithm

$$V_{C1}^{\text{ref}} = V_{\text{MPP}}. \tag{4}$$

The control of V_{C1} is done using double-loop control, employing an outer voltage and inner current control loop that generates d_{SC}. The control loop for V_{PV} is given in Fig. 4.

2) Control of S_3-S_6: The switches S_3-S_6 are operated to control the battery current I_{batt}, like an interleaved boost converter. The duty ratio of S_3, S_5 is d_1, and S_4, S_6 are switched complimentary to S_3 and S_5, respectively (with a small dead time). The gate pulses for S_3 and S_5 are shifted by 180°. Fig. 5(a) shows the gate signals for S_3-S_6 and the current in

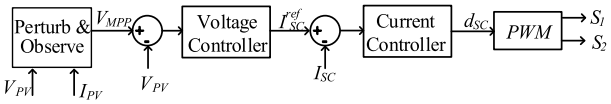

Fig. 4. PV voltage control loop.

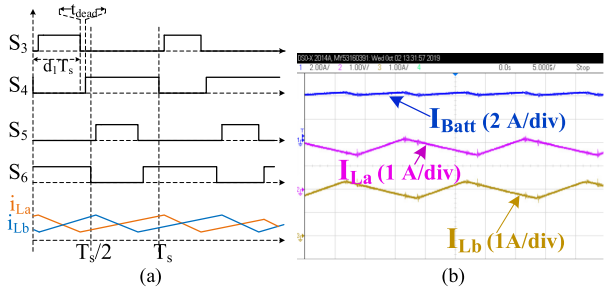

Fig. 5. (a) Gate pulses for switches S_3-S_6 and currents in L_a and L_b. (b). Experimental waveforms for i_{La}, i_{Lb}, and i_{batt}.

inductors L_a and L_b. I_{batt} is the sum of currents in L_a and L_b and is having low ripple content, as seen in the experimental waveform in Fig. 5(b). The duty ratio, d_1 is obtained using a PI controller, aimed to control the battery current to its reference value I_b^{ref} which is explained below. Due to the volt-second balance across L_a and L_b, the steady-state value of d_1 is

$$d_1 = V_{\text{batt}}/V_{\text{PV}}. \tag{5}$$

The battery supplies the power difference between solar power and the load demand. There is one more component of battery power, which is the power required to charge the SC. $I_{\text{SC,ch}}$ the charging current of the SC is proportional to the difference between the SC instantaneous voltage v_{SC}, and the maximum voltage $v_{\text{sc}}^{\max}$. However, to prevent high charging current from being reflected to the battery side when the v_{SC} is very low, I_{SC} is limited to a maximum value

$$\therefore I_{\text{SC}} = \max\left(I_{\text{SC}}^{\max}, k_1\left(v_{\text{SC}}^{\max} - v_{\text{sc}}\right)\right). \tag{6}$$

The battery power is given by (neglecting the losses)

$$P_{\text{batt}} = P_{\text{load}} - P_{\text{PV}} + P_{\text{SC}} \tag{7}$$

where

$$P_{\text{SC}} = V_{\text{SC}} I_{\text{SC}} \tag{8}$$

where P_{load} is the load power, P_{PV} is the power generated by the PV, and P_{SC} is the power required to charge the SC. I_{batt} is changed toward the final value slowly to prevent it from experiencing a fast change. The final value of the I_{batt} is

$$I_b^f = P_{\text{batt}}/V_{\text{batt}} \tag{9}$$

where V_{batt} is the battery voltage. The reference for I_{batt} is changed slowly from its initial value to its final value I_b^f.

$$\therefore I_b^{\text{ref}} = I_b^0 + k_1 \int \left(I_b^f - I_b\right) dt \tag{10}$$

where I_b^0 is the initial value of I_b^{ref} and I_b^f is the final value. k_1 determines how fast I_{batt} tracks the reference. A large value of k_1 makes I_{batt} rise fast, but a low value of k_1 requires a

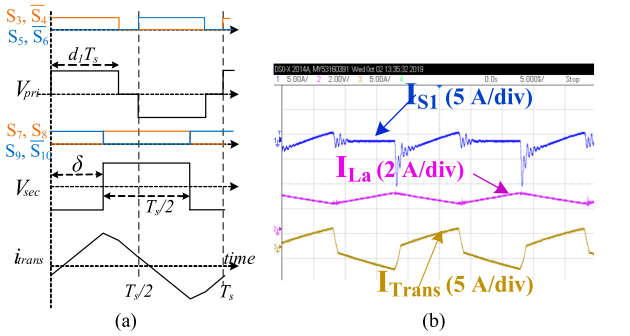

Fig. 6. (a) Gate pulses for switches S_7-S_{10}, transformer voltages, and current. (b) Experimental waveforms of switch currents, i_{La} and i_{trans}.

higher capacity SC. Therefore, the value of k_1 must be chosen to optimize the SC size and the maximum rate at which the I_{batt} can be changed without causing life deterioration. When v_{SC} reaches its maximum $V_{\text{sc}}^{\max}$, SC cannot be charged anymore. So, $I_{\text{SC,ch}}$ is made zero. Also, I_{batt} cannot be slowed down i.e., I_b^{ref} should be equal to I_b^f, to prevent the overcharging of SC.

3) Control of S_7-S_{10}: The switches S_7-S_{10}, form the secondary side inverter of the DAB converter and are controlled to regulate the load voltage using phase shift control. The duty ratio of the gate pulses for these switches is 0.5 and they are displaced by an angle δ from the gate pulses of S_3-S_6. The gate pulse for S_7 is displaced from the gate pulse for S_3 by δ, S_8 is displaced by δ from the gate pulse of S_4, and so on. δ determines the power transfer across the DAB, and thus regulates the load voltage. Its value is obtained from a PI controller, which regulates the error in load voltage to zero. By switching S_3-S_{10}, phase displaced square/quasi-square voltages are generated at the primary and secondary windings of the transformer as shown in Fig. 6(a). The transformer primary and secondary voltages and transformer primary currents are shown in Fig. 6(b). The control loops for load voltage and battery current control are shown in Fig. 7(a) and (b) respectively.

IV. ZVS, Current Stress, and Loss Analysis

In this section, the ZVS region and current stress in the switches are analyzed using a mathematical model of CF-DAB. Since the SC acts only during transient conditions, its operation can be ignored for the loss analysis. The analysis presented here will consider only the CF-DAB part, which includes the battery, PV source, and load. The values presented in this section are normalized using the following base values:

$$P_{\text{base}} = \left(\frac{4}{\pi}\right)^2 \frac{V_1 V_2}{4\pi f L n},\ V_{\text{base}} = V_{\text{batt}},\ i_{\text{base}} = \frac{P_{\text{base}}}{V_{\text{base}}} \tag{11}$$

where V_1 and V_2 are the nominal values of V_{C1} and V_{DC} respectively.

A. Modeling of CF-DAB

A DAB converter can be modeled as two HF alternating square/quasi square voltage sources on the primary and secondary sides of the transformer. The transformer resistance and

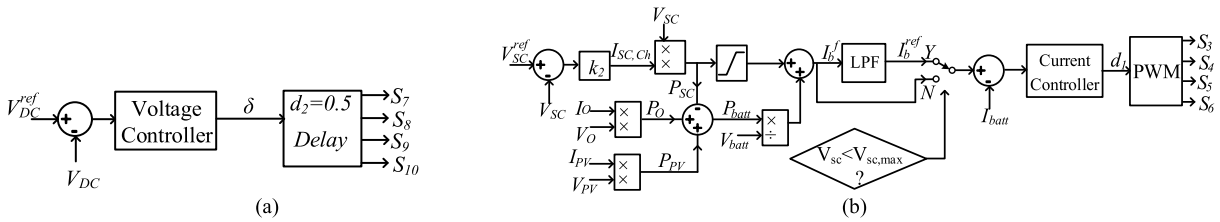

Fig. 7. Control scheme for the proposed system. (a) Output voltage control loop. (b) SC charging and battery current control loop.

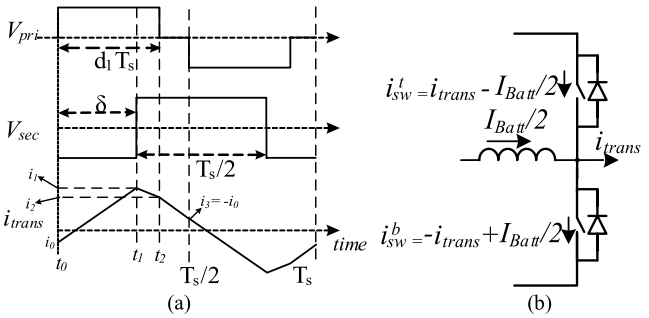

Fig. 8. (a) Waveforms of transformer primary and secondary voltages and currents. (b) Switch currents in the primary side switches.

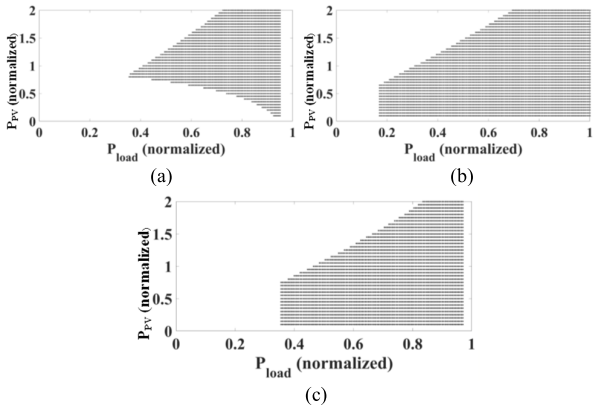

Fig. 9. Region of ZVS in the proposed MPC (a) $V_{PV} = 1.67\ V_{batt}$. (b) $V_{PV} = 2\ V_{batt}$. (c) $V_{PV} = 2.33\ V_{batt}$.

the magnetizing current at HF can be neglected, and the current waveform can be approximated as a piecewise linear function as shown in Fig. 8(a) [27]–[29]. The figure is shown for only the case $d_1 < 0.5$. The case $d_1 > 0.5$ can be analyzed similarly. The values of currents i_0, i_1, and i_2 shown in Fig. 8(a) can be determined by solving the following:

$$i_1 = i_0 + \frac{V_{\text{pri}}(t_0^+) - V_{\text{sec}}(t_0^+)}{L}(t_1 - t_0) \tag{12}$$

$$i_2 = i_1 + \frac{V_{\text{pri}}(t_1^+) - V_{\text{sec}}(t_1^+)}{L}(t_2 - t_1) \tag{13}$$

$$i_3 = -i_0. \tag{14}$$

These values are needed to analyze the ZVS behavior of the MPC. $V_{\text{pri}}(t^+)$ and $V_{\text{sec}}(t^+)$ are the values of the primary and secondary voltages, immediately after the time instant, t.

B. ZVS Behavior of the MPC

One of the main advantages of DAB topologies is the ability to undergo ZVS under certain conditions. The occurrence of ZVS depends on the magnitude and direction of current in the switches which is the same as the transformer current at the instant of switching (in voltage fed DAB). In a CF-DAB, the primary side switches carry the transformer current as well as the current in L_a (L_b) as shown in Fig. 8(b). Due to this, ZVS behavior is changed from that of a conventional DAB. The range of load and PV power for which the MPC undergoes ZVS is analyzed here. The conditions under which ZVS occurs in a power electronic switch can be summarized as [27]

Switch current before turn-on, $i_{\text{ON}} < 0$ (15.a)

(anti-parallel diode of switch conducts)

Switch current at the instant of turn-off, $i_{\text{OFF}} > 0$. (15.b)

For the devices of the primary side HF inverter, the switch currents while conducting are given by

$$i_{\text{SW}}^t = i_{\text{trans}} - I_{\text{batt}}/2 \tag{16}$$

$$i_{\text{SW}}^b = -i_{\text{trans}} + I_{\text{batt}}/2. \tag{17}$$

The values of i_{ON} and i_{OFF} can be determined by solving (12)–(14) for each value of load power and PV power in discrete steps and analyzing the devices that are conducting. Solving (12)–(14) and checking for (15.a) and (15.b), it can be verified that whether the operating point (P_{load}, P_{PV}) satisfies ZVS or not. If the ZVS conditions are satisfied, the point falls under the ZVS zone. This is performed for three values of V_{PV} relative to V_{batt} (1.67_t, 2, and 2.33 V_{batt}) and those regions are shown by the shaded zone in Fig. 9.

It can be inferred from the figure that when V_{PV} is equal to twice the battery voltage, i.e., $d_1 = 0.5$, ZVS occurs over a wide region, whereas for other values of the PV voltage, the ZVS region is narrowed down. So from a switching loss point of view, it is preferred to keep the nominal MPP voltage of the PV panel equal to twice the battery voltage.

C. Switch Current Stress

The rms value of the switch current can be calculated using the values of i_0, i_1, i_2 obtained from (12)–(14). Equations (16), (17) can be used to determine the total switch current, and calculating the rms values of the total switch current over a cycle gives the total switch current stress. Fig. 10 shows the plots of total switch rms current stress including all the switches versus P_{PV} for P_{load} equal to 0.4 and 0.8 p.u. It can be

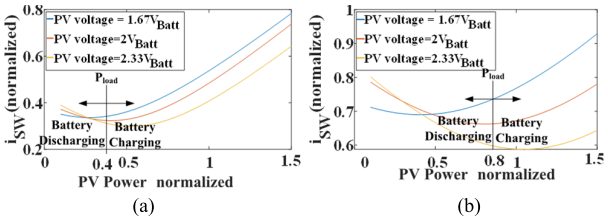

Fig. 10. Plots of total switch rms current (normalized) versus PV power (a) $P_{\text{load}} = 0.4$ PU. (b) $P_{\text{load}} = 0.8$ PU.

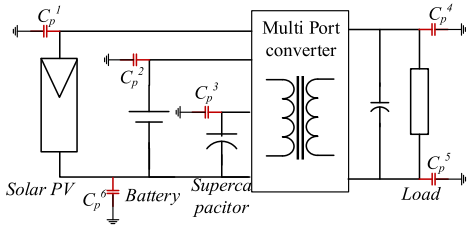

Fig. 11. Parasitic capacitances at the various points concerning sources and loads.

seen that the switch current stress heavily depends on the P_{load}, and is lower when the P_{load} and P_{PV} are close to each other. As the P_{load} and P_{PV} deviate more and more from each other, switch current stress increases. Also, switch current stress is higher at lower values of V_{PV}.

D. Total Loss Calculation

Total losses in the circuit can be calculated by adding the individual loss components. If the operation falls in the ZVS zone, switching loss can be neglected, otherwise, they can be taken equal to [28]

$$P_{\text{sw}} = 0.5 C_{\text{dev}} V_{\text{dev}}^2 f_{\text{sw}} \tag{18}$$

where V_{dev} is the blocking voltage of the device and C_{dev} is the device's effective output capacitance at the blocking voltage. Switching losses for all devices (primary side and secondary side) can be added to determine the total switching loss. The device's conduction losses can be determined by using the device's rms current stress and their ON-state resistance. Transformer copper loss can be determined by calculating the rms value of transformer current using the values i_0, i_1, and i_2 for a particular load using the following:

$$i_{T,\text{rms}} = \sqrt{\frac{\left(i_0^2 + i_0 i_1 + i_1^2\right)(t_1 - t_0) + \left(i_1^2 + i_1 i_2 + i_2^2\right) \times (t_2 - t_1) + \left(i_2^2 + i_2 i_3 + i_3^2\right)(t_3 - t_2)}{1.5}}. \tag{19}$$

The resulting transformer copper loss can be calculated as

$$P_{\text{Cu}}^T = i_{T,\text{rms}}^2 R_{\text{trans}}. \tag{20}$$

Transformer core loss can be calculated from the core's datasheet using the information provided. Losses in inductors L_a and L_b, P_{Lab} can be calculated by using their dc resistances and the operating value of battery current.

Total losses can be obtained by the addition of all the above-mentioned components. It should be noted that since the SC acts only during transients, and once the transients are over and steady-state is reached, SC converter (S_1, S_2, L_{SC}) is not active ($i_{\text{LSC}} \approx 0$), losses in the SC converter can be neglected. However, switching loss taking place in the SC converter needs to be accounted for, which can be calculated using (18); the value of V_{dev} for SC circuit is equal to V_{PV}.

E. Ground Leakage Current

Ground leakage current arises due to the parasitic capacitance that exists between the various nodes and ground as shown in Fig. 11. Due to the switchings, the voltages at these nodes oscillate, and thus capacitive current flows through these parasitic capacitances that manifest as ground leakage current. The parasitic capacitance for lumped sources like battery and SC are of the order of a few picofarads, whereas for the solar PV array, these capacitances are of the order of hundreds of nanofarads owing to their large size [30]. It should be noted that the leakage current is very low under the following two cases.

1) When the ground terminals of source and load are tied together [31].
2) When there is galvanic isolation between the load and the source [32].

If there is no galvanic isolation between the source and load, and the source and load negative (ground) terminals are not tied together (e.g., a full bridge transformer-less inverter), there will be a significant leakage current. In the system proposed in this article, the sources are having a common negative terminal, and the load is galvanically isolated through an HF transformer. So the above-mentioned conditions are satisfied and thus the ground leakage current is not high.

V. System Design and Parameter Selection

The system design depends on the requirements and availability of the available resources. To select the required parameters of the system, the inputs can be taken as the required load voltage, available battery voltage, and voltage rating of the solar PV.

A. SC Capacity and Voltage Rating

The SC capacity is selected based on the expected power transients, which can be due to either a load change or a change in solar insolation. Since the SC is interfaced to the PV through a buck-boost system, with PV on the higher voltage side, the maximum v_{SC} will be equal to the maximum PV voltage. So, SC voltage rating can be taken as the maximum expected PV voltage as follows:

$$V_{\text{SC}}^{\text{rated}} = V_{\text{PV}}^{\text{max}}. \tag{21}$$

SC rating is determined by the peak power demand. This can be determined from the load and generation characteristics and can be translated to the required transient energy (E_{trans}). A low SC capacity will lead to transient power being reflected on the battery side whereas too high a value of SC capacity

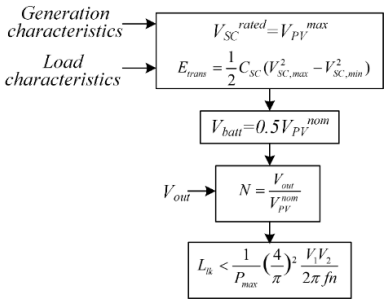

Fig. 12. Design rules for the proposed system.

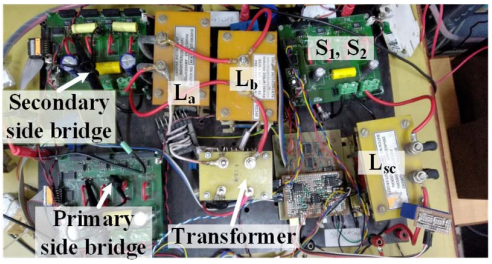

Fig. 13. Laboratory prototype of proposed MPC.

TABLE III
PARAMETERS OF EXPERIMENTAL SETUP

	Quantity	Value
V_{out}	Load Voltage	100 V
V_{Batt}	Battery Voltage	24 V
C_{SC}, V_{SC}	Supercapacitor capacity and voltage	2.8 F, 48 V
n	Transformer turns ratio	2.8
L_m	Transformer Magnetizing Inductance	700 μH
L_a, L_b	Battery side inductors	250 μH
L_{SC}	SC side inductor	250 μH
C_1	PV side Capacitor	1100 μF
C_2	Load side Capacitor	500 μF
f	Switching Frequency	50 kHz
Solar Panel	EPS PV Emulator	
Low voltage side devices	FDP2572, 150V, 29A MOSFET	
High voltage side devices	FDPF14N30, 300V, 14A MOSFET	

will not be economically optimum. The SC capacity can be calculated by

$$E_{SC} >= E_{trans} = \frac{1}{2} C_{SC}\left(V_{SC,max}^2 - V_{SC,min}^2\right). \quad (22)$$

where $V_{SC,max}$ and $V_{SC,min}$ are the maximum and minimum limit of the SC operating voltage.

B. Battery Voltage Rating and Capacity

It can be seen from Fig. 9 that when $V_{PV} = 2\ V_{batt}$, ZVS takes place over a wide region, which is desirable. So the battery nominal voltage can be taken as half of the nominal value of MPP voltage of the solar PV panel.

The battery is used to supply power when solar power generation is low/absent, so the battery rating (in Ah/kWh) can be calculated as the net difference between generation and consumption, and this can be determined from load and generation profiles. The above-described design criteria are the basic philosophy of a HESS design. The design of a practical system takes into consideration several other factors such as frequency response of the battery and SC, cost, and so on. The optimum design of HESS is a vast topic in itself and is outside the scope of this article.

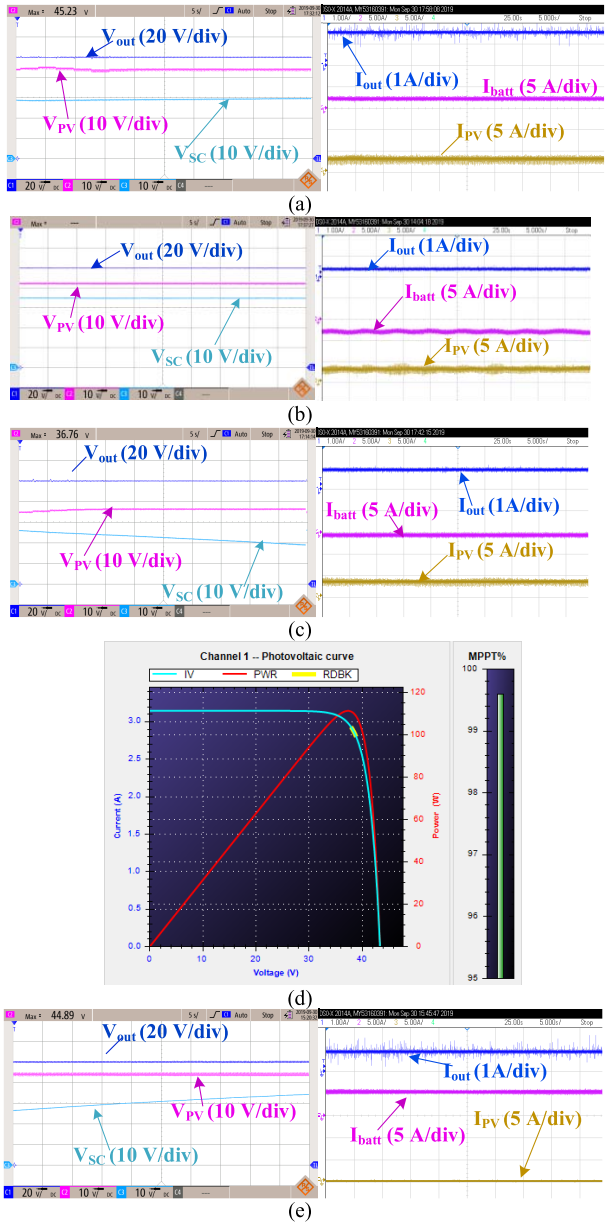

Fig. 14. Experimental waveforms under static conditions (constant load and solar generation). (a) PV and battery supplying power to load. (b) PV supplying power to battery and load. (c) MPP tracking of solar PV. (d) PV curve display showing MPP performance. (e) MPC operation without PV.

C. Transformer Turns Ratio

It is a well-known fact that the optimum operation of a DAB takes place at unity voltage gain because when the voltages on the two sides of the transformer are matched, ZVS takes place over a wide power range and current stress is also minimum. So the transformer turns ratio can be set to give a unity gain at the nominal values of V_{DC} and V_{PV}

$$n = \frac{V_{out}}{V_{PV}^{nom}}. \quad (23)$$

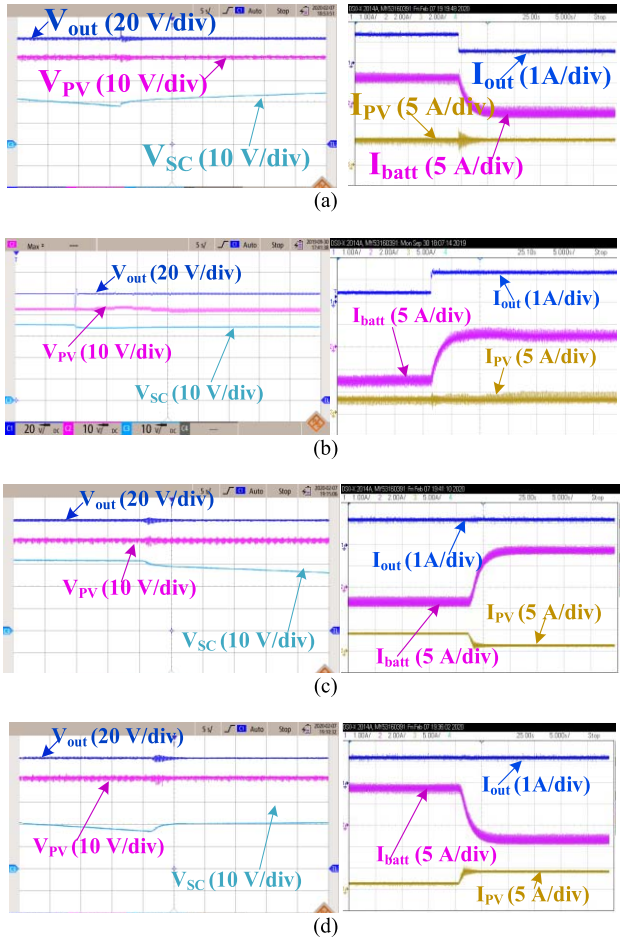

Fig. 15. Experimental waveforms under dynamic conditions with changing loads and solar generation. Changeover of battery current from (a) positive (discharging) to negative (charging) due to decrease in load (b) negative (charging) to positive (discharging) due to increase in load. Switch-over of battery current from (c) negative (charging) to positive (discharging) value due to decrease in solar irradiation (d) positive (discharging) to negative (charging) value due to increase in solar irradiation.

D. Leakage Inductance of the Transformer

It is desirable to have a large leakage inductance to have better control over the power flow, but too large a value of L_{lk} limits the power transfer capability of the converter (3). The maximum value of permissible leakage inductance is

$$L_{lk} < \frac{1}{P_{\max}}\left(\frac{4}{\pi}\right)^2 \frac{V_1 V_2}{2\pi f n}. \tag{24}$$

But, L_{lk} should be much smaller than this value to account for resistance and variation in duty ratio d_1. The design process is summarized in Fig. 12.

VI. Laboratory Prototype and Experimental Results

A proposed scheme has been validated on a laboratory prototype with parameters listed in Table III. A photograph of the MPC used is shown in Fig. 13. The converter has been tested to validate its performance under various static and dynamic conditions.

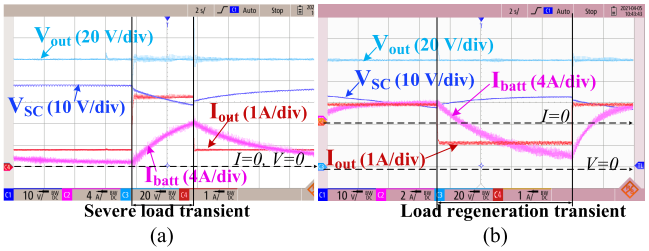

Fig. 16. Experimental waveforms under. (a) Severe load transients. (b) Regenerative transient.

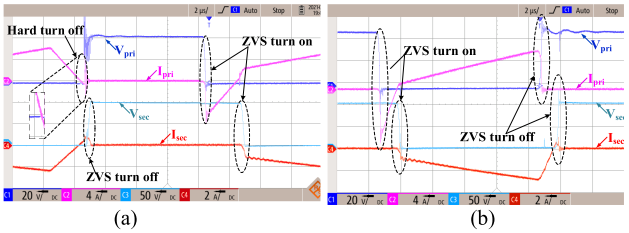

Fig. 17. Experimental waveforms showing primary side and secondary side devices undergoing hard switching and ZSV when the operating point lies in respective zone. (a) Hard switching at $V_{\text{VP}} = 1.667\ V_{\text{batt}}$, $P_{\text{load}} = 0.3$, $V_{\text{PP}} = 0.4$ P.U. (b) ZVS at $V_{\text{PV}} = 2\ V_{\text{batt}}$, $P_{\text{load}} = 0.3$, $P_{\text{PV}} = 0.4$ P.U.

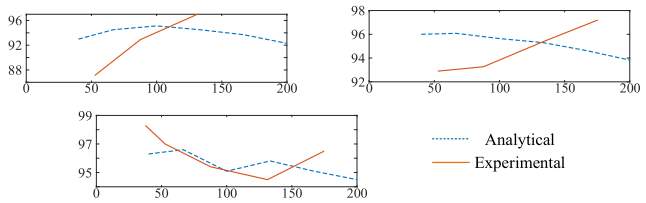

Fig. 18. Analytical and experimental efficiency curve of the laboratory prototype for three values of P_{PV}.

TABLE IV
VALUES OF LEAKAGE CURRENT MEASURED AT VARIOUS NODES IN THE PROPOSED SYSTEM EXPERIMENTAL SETUP

Capacitance and their location	Capacitance value	Leakage current (rms)
PV positive to ground, $C_P{}^1$	200 nF	12.9 mA
Battery positive to ground $C_P{}^2$	1 nF	8.4 mA
Supercapacitor positive to ground $C_P{}^3$	1 nF	11 mA
Load Positive to ground, $C_P{}^4$	1 nF	10.8 mA
Load negative to ground, $C_P{}^5$	1 nF	10.8 mA
Common sources negative (PV, battery, SC) to ground, $C_P{}^6$	200 nF	11.3 mA

*Capacitances $C_p{}^1$, $C_p{}^2$ etc. are at the locations shown in Fig. 11.

Fig. 14(a) shows the waveforms when the solar PV and battery are supplying power to the load. In this case, the load demand (170 W) is higher than P_{MPP} (135 W) of the solar panel. So, the battery is in the discharging mode, supplying the balance load power. Fig. 14(b) shows the case when P_{MPP} is higher than the load demand (50 W), so the battery is being charged with surplus power. Fig. 14(c) shows the MPPT tracking performance of the converter. MPPT is performed by making the reference voltage for C_1 equal to V_{MPP}. V_{MPP} is obtained using *perturb and observe* algorithm. To eliminate the oscillations in V_{PV} (once V_{MPP} is reached),

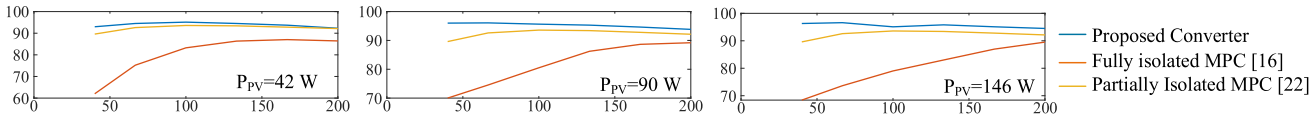

Fig. 19. Efficiencies of various MPC topologies reported.

TABLE V
COMPARISON OF THE PROPOSED MPC WITH OTHER MPC CONFIGURATIONS REPORTED IN LITERATURE

MPC architecture	Switch count[a]/ No. of ports	Transformer rating	No. of inductors	Isolation of PV from load	No. of Power conversion stage		
					RES to load	Battery to load	PV to Battery
Non-isolated [14]	7/3	-	3	No	1	1	1
Fully isolated [16]	12/3	P_{load}+P_{Batt}	1 (filter for battery)	Yes	1	1	1
Partially isolated [22]	10/4	P_{load}	3	Yes	2	2	1
Proposed	10/4	P_{load}	3	Yes	1	1	1

[a] Switch count considering full bridge operation, including diodes (antiparallel diodes of switches are not considered).

the increment in V_{PV} at each time step is made adaptive. It can be seen that V_{PV} gradually becomes equal to 38 V, which is the V_{MPP} setting of the PV emulator. This can be seen in the PV curve display of the PV emulator which is shown in Fig. 14(d). Fig. 14(e) shows the waveforms when the system is operated without solar PV, only on battery power, i.e., under very low or no insolation conditions. Capacitor C_1 voltage is regulated to 45 V which is the open-circuit voltage of PV, and the load under this condition is 100 W. This demonstrates the scheme working under very low irradiation conditions.

Fig. 15(a) and (b) shows the waveforms under dynamic conditions when the load is changed from high to low and vice versa. The seamless transition of I_{batt} from positive (discharging) to negative and vice versa as the load changes can be seen. I_{batt} changes slowly because of the battery current control. Because I_{batt} does not immediately track load demand, but rather changes slowly, the difference in power is supplied by the SC. This effect can be seen from the change in SC voltage. As I_{out} reduces, v_{SC} rises and vice versa. Fig. 15(c) and (d) shows the converter operation under dynamic PV conditions i.e., when PV irradiation is changed from high (100% insolation) to low (65%) value and vice versa, while the load is kept fixed to 90 W. The impact of a sudden change in insolation is translated into a gradual change in the battery current from -2 A to 3 A. Here also, change in I_{batt} takes place slowly. This shows the effectiveness of the SC and the scheme to deal with sudden changes in solar irradiation and load to prevent the deterioration of battery life.

In Fig. 16(a), the load is given a step change from 80 to 350 W for 4 s to simulate a severe load transient. The effect of transient on battery current can be seen that even with such a change in load, battery current does not go to very high and in fact, it is the SC that is supplying load during this transient. In Fig. 16(b), the load current changes from 0.8 to -1 A which indicates a load regenerating transient. Battery current slowly goes to negative and most of the regenerative power is taken by the SC.

Fig. 17(a) shows the device voltage and current waveforms when P_{PV} is equal to 132 W, V_{PV} is 40 V, and P_{load} is 177 W. According to Fig. 9(a), this point does not fall under the ZVS zone, and this is confirmed by the experimental results which show primary side device undergoing hard switching. When V_{PV} is changed to 48 V, the resulting operating point falls under the ZVS zone and this is confirmed by the experimental waveforms as well. Fig. 18 shows the analytical and experimental efficiency curve of the laboratory prototype for three values of solar insolation for a PV voltage of 40 V. It can be seen that the efficiency of MPC is over 94% for a wide range of loads, even in the event of variation in insolation. To measure the ground leakage current in the experimental setup, we put capacitances from the different nodes to the ground as shown in Fig. 11, and measured the current through them. The values are indicated in Table IV.

VII. CONCLUSION

A new approach for interfacing a battery, SC, PV generation, and load using a CF-DAB-based MPC is proposed and validated in this article. The proposed approach makes use of SC for MPPT of RES, thus protecting the battery from load transients as well as transients arising from RES. Using this approach, MPPT can be performed even with a highly degraded battery, which is otherwise not possible when MPPT is performed using the battery alone. Thus, the inclusion of SC, in addition to enhancing the lifetime of the battery, also enhances the system's reliability. The operating region for which ZVS takes place in the DAB switches of the adopted converter structure was analyzed and it was found that for $V_{PV} = 2\ V_{batt}$, the converter operates under ZVS for a wide range of loads. All the objectives for the system under consideration were achieved and demonstrated, which include implementing MPPT of RES, battery current control and regulation of load voltage. Under the dynamic load/source conditions, the MPC slows down the rate of change of battery current thus helping in lowering lifetime deterioration of the battery. The main energy paths, i.e., from PV to battery and from the battery to load are all single-stage power conversion,

which helps in minimizing the number of switches and enables the converter to operate at high efficiency. The performance of the converter was tested experimentally under various loading and irradiation conditions and was observed to operate satisfactorily under steady state and transient conditions. Table V shows a comparison of the proposed system with similar MPC topologies proposed in the literature and their efficiency comparison is done using PLECS simulation as shown in Fig. 19. It can be seen that the proposed system reduces the number of switches as compared to similar solutions and also gives higher efficiency.

REFERENCES

[1] B. Vulturescu, S. Butterbach, and C. Forgez, "Experimental considerations on the battery lifetime of a hybrid power source made of ultracapacitors and lead-acid batteries," *IEEE J. Emerg. Sel. Topics Power Electron.*, vol. 2, no. 3, pp. 701–709, Sep. 2014.

[2] E. Chemali, M. Preindl, P. Malysz, and A. Emadi, "Electrochemical and electrostatic energy storage and management systems for electric drive vehicles: State-of-the-art review and future trends," *IEEE J. Emerg. Sel. Topics Power Electron.*, vol. 4, no. 3, pp. 1117–1134, Sep. 2016, doi: 10.1109/JESTPE.2016.2566583.

[3] V. Bolborici, F. P. Dawson, and K. K. Lian, "Hybrid energy storage systems: Connecting batteries in parallel with ultracapacitors for higher power density," *IEEE Ind. Appl. Mag.*, vol. 20, no. 4, pp. 31–40, Jul./Aug. 2014, doi: 10.1109/MIAS.2013.2288374.

[4] Q. Zhang and G. Li, "Experimental study on a semi-active battery-supercapacitor hybrid energy storage system for electric vehicle application," *IEEE Trans. Power Electron.*, vol. 35, no. 1, pp. 1014–1021, Jan. 2020, doi: 10.1109/TPEL.2019.2912425.

[5] A. Kuperman, I. Aharon, S. Malki, and A. Kara, "Design of a semi-active battery-ultracapacitor hybrid energy source," *IEEE Trans. Power Electron.*, vol. 28, no. 2, pp. 806–815, Feb. 2013.

[6] L. Gao, R. A. Dougal, and S. Liu, "Power enhancement of an actively controlled battery/ultracapacitor hybrid," *IEEE Trans. Power Electron.*, vol. 20, no. 1, pp. 236–243, Jan. 2005, doi: 10.1109/TPEL.2004.839784.

[7] N. R. Tummuru, M. K. Mishra, and S. Srinivas, "Dynamic energy management of renewable grid integrated hybrid energy storage system," *IEEE Trans. Ind. Electron.*, vol. 62, no. 12, pp. 7728–7737, Dec. 2015.

[8] S. Kurm and V. Agarwal, "A multi input converter for interfacing battery and supercapacitor to the load," in *Proc. IEEE Ind. Appl. Soc. Annu. Meeting (IAS)*, Portland, OR, USA, Sep. 2018, pp. 1–6.

[9] S. Kurm and V. Agarwal, "Hybrid energy storage system based on a novel reduced rating multi input converter," *IEEE Trans. Power Electron.*, vol. 35, no. 11, pp. 12133–12142, Nov. 2020, doi: 10.1109/TPEL.2020.2987833.

[10] A. C. Nair, M. J. Vishal, and B. G. Fernandes, "A quad active bridge based on-board power electronic interface for an electric vehicle," in *Proc. IEEE Energy Convers. Congr. Expo. (ECCE)*, Portland, OR, USA, Sep. 2018, pp. 5941–5947.

[11] Z. Wang, Q. Luo, Y. Wei, D. Mou, X. Lu, and P. Sun, "Topology analysis and review of three-port DC–DC converters," *IEEE Trans. Power Electron.*, vol. 35, no. 11, pp. 11783–11800, Nov. 2020, doi: 10.1109/TPEL.2020.2985287.

[12] W. Jiang and B. Fahimi, "Multiport power electronic interface—Concept, modeling, and design," *IEEE Trans. Power Electron.*, vol. 26, no. 7, pp. 1890–1900, Jul. 2011.

[13] P. Prabhakaran and V. Agarwal, "Novel four-port DC–DC converter for interfacing solar PV–fuel cell hybrid sources with low-voltage bipolar DC microgrids," *IEEE J. Emerg. Sel. Topics Power Electron.*, vol. 8, no. 2, pp. 1330–1340, Jun. 2020, doi: 10.1109/JESTPE.2018.2885613.

[14] R. Faraji, H. Farzanehfard, G. Kampitsis, M. Mattavelli, E. Matioli, and M. Esteki, "Fully soft-switched high step-up nonisolated three-port DC–DC converter using GaN HEMTs," *IEEE Trans. Ind. Electron.*, vol. 67, no. 10, pp. 8371–8380, Oct. 2020, doi: 10.1109/TIE.2019.2944068.

[15] E. Asa, K. Colak, M. Bojarski, and D. Czarkowski, "Asymmetrical duty-cycle and phase-shift control of a novel multiport CLL resonant converter," *IEEE J. Emerg. Sel. Topics Power Electron.*, vol. 3, no. 4, pp. 1122–1131, Dec. 2015, doi: 10.1109/JESTPE.2015.2408565.

[16] Y. Wang, F. Han, L. Yang, R. Xu, and R. Liu, "A three-port bidirectional multi-element resonant converter with decoupled power flow management for hybrid energy storage systems," *IEEE Access*, vol. 6, pp. 61331–61341, 2018, doi: 10.1109/ACCESS.2018.2872683.

[17] J. Zeng, W. Qiao, L. Qu, and Y. Jiao, "An isolated multiport DC–DC converter for simultaneous power management of multiple different renewable energy sources," *IEEE J. Emerg. Sel. Topics Power Electron.*, vol. 2, no. 1, pp. 70–78, Mar. 2014, doi: 10.1109/JESTPE.2013.2293331.

[18] S. Kurm and V. Agarwal, "Current fed dual active bridge based multi-port DC/AC converter for standalone solar PV fed systems with battery backup," in *Proc. IEEE Int. Conf. Power Electron., Drives Energy Syst. (PEDES)*, Jaipur, India, Dec. 2020, pp. 1–6, doi: 10.1109/PEDES49360.2020.9379447.

[19] H. Wu, K. Sun, L. Zhu, and Y. Xing, "An interleaved half-bridge three-port converter with enhanced power transfer capability using three-leg rectifier for renewable energy applications," *IEEE J. Emerg. Sel. Topics Power Electron.*, vol. 4, no. 2, pp. 606–616, Jun. 2016, doi: 10.1109/JESTPE.2015.2478140.

[20] Z. Qian, O. Abdel-Rahman, H. Al-Atrash, and I. Batarseh, "Modeling and control of three-port DC/DC converter interface for satellite applications," *IEEE Trans. Power Electron.*, vol. 25, no. 3, pp. 637–649, Mar. 2010.

[21] P. Kolahian, H. Tarzamni, A. Nikafrooz, and M. Hamzeh, "Multi-port DC–DC converter for bipolar medium voltage DC micro-grid applications," *IET Power Electron.*, vol. 12, no. 7, pp. 1841–1849, 2019.

[22] B. Mangu *et al.*, "Grid-connected PV-wind-battery-based multi-input transformer-coupled bidirectional DC–DC converter for household applications," *IEEE J. Emerg. Sel. Topics Power Electron.*, vol. 4, no. 3, pp. 1086–1095, Sep. 2016.

[23] Y. Lu, K. Sun, H. Wu, X. Dong, and Y. Xing, "A three-port converter based distributed DC grid connected PV system with autonomous output voltage sharing control," *IEEE Trans. Power Electron.*, vol. 34, no. 1, pp. 325–339, Jan. 2019, doi: 10.1109/TPEL.2018.2822726.

[24] X. Sun, Y. Shen, W. Li, and H. Wu, "A PWM and PFM hybrid modulated three-port converter for a standalone PV/battery power system," *IEEE J. Emerg. Sel. Topics Power Electron.*, vol. 3, no. 4, pp. 984–1000, Dec. 2015.

[25] Z. Ding, C. Yang, Z. Zhang, C. Wang, and S. Xie, "A novel soft-switching multiport bidirectional DC–DC converter for hybrid energy storage system," *IEEE Trans. Power Electron.*, vol. 29, no. 4, pp. 1595–1609, Apr. 2014, doi: 10.1109/TPEL.2013.2264596.

[26] S. Kurm and V. Agarwal, "Novel dual active bridge based multi port converter for interfacing hybrid energy storage systems in electric vehicles," in *Proc. IEEE Transp. Electrific. Conf.*, Bengaluru, India, Dec. 2019, pp. 1–5, doi: 10.1109/ITEC-India48457.2019.ITECINDIA2019-223.

[27] F. Krismer and J. W. Kolar, "Efficiency-optimized high-current dual active bridge converter for automotive applications," *IEEE Trans. Ind. Electron.*, vol. 59, no. 7, pp. 2745–2760, Jul. 2012, doi: 10.1109/TIE.2011.2112312.

[28] G. G. Oggier, G. O. García, and A. Oliva, "Switching control strategy to minimize dual active bridge converter losses," *IEEE Trans. Power Electron.*, vol. 24, no. 7, pp. 1826–1838, Jul. 2009, doi: 10.1109/TPEL.2009.2020902.

[29] V. N. S. R. Jakka, A. Shukla, and G. D. Demetriades, "Dual-transformer-based asymmetrical triple-port active bridge (DT-ATAB) isolated DC–DC converter," *IEEE Trans. Ind. Electron.*, vol. 64, no. 6, pp. 4549–4560, Jun. 2017, doi: 10.1109/TIE.2017.2674586.

[30] SMA Solar Technical Information. *Leading Leakage Currents: Information on the Design of Transformerless Inverters of Type Sunny Boy, Sunny Tripower, Sunny Highpower*. Accessed: Aug. 10, 2021. [Online]. Available: https://files.sma.de/downloads/Ableitstrom-TI-en-26.pdf

[31] Y. P. Siwakoti and F. Blaabjerg, "H-bridge transformerless inverter with common ground for single-phase solar-photovoltaic system," in *Proc. IEEE Appl. Power Electron. Conf. Expo. (APEC)*, Tampa, FL, USA, Mar. 2017, pp. 2610–2614, doi: 10.1109/APEC.2017.7931066.

[32] Ó. López *et al.*, "Eliminating ground current in a transformerless photovoltaic application," *IEEE Trans. Energy Convers.*, vol. 25, no. 1, pp. 140–147, Mar. 2010, doi: 10.1109/TEC.2009.2037810.